Microstructural and textural investigation of an Mg–Dy alloy after hot plane strain compression

Fairouze Guerza-Soualah, Hiba Azzeddine, Thierry Baudin, Anne-Laure Helbert, Francois Brisset, Djamel Bradai

Available online at www.sciencedirect.com

ScienceDirect

Journal of Magnesium and Alloys 8 (2020) 1198–1207

www.elsevier.com/locate/jma

Full Length Article

Microstructural and textural investigation of an Mg–Dy alloy after hot plane strain compression

Fairouze Guerza-Soualah[a], Hiba Azzeddine[b,*], Thierry Baudin[c], Anne-Laure Helbert[c], François Brisset[c], Djamel Bradai[a]

[a] *Laboratory of Materials Physics, Faculty of Physics, University of Sciences and Technology - Houari Boumediene (U.S.T.H.B.), P.O. Box 32, El- Alia, Bab-Ezzouar, DZ-16111, Algiers, Algeria*

[b] *Faculty of Technology, University of Mohamed Boudiaf, M'Sila 28000, Algeria*

[c] *CNRS, Institut de Chimie Moléculaire et des Matériaux d'Orsay, Université Paris-Saclay, 91405 Orsay, France*

Received 14 February 2020; received in revised form 18 May 2020; accepted 28 May 2020
Available online 24 June 2020

Abstract

The microstructure and texture development in a Mg–0.41Dy (wt%) alloy after plane strain compression (PSC) at 300 °C under a strain rate of 10^{-2} and 10^{-4} s^{-1} up a final true strain of −1.2 were investigated using electron backscatter diffraction (EBSD) and X-ray diffraction. At high strain rate of 10^{-2} s^{-1}, the microstructure exhibited massive twins mainly $\{10\bar{1}2\}$ extension, $\{10\bar{1}1\}$ contraction and $\{10\bar{1}3\}$-$\{10\bar{1}2\}$ double twin due to the random texture of the as-cast alloy. Meanwhile, at a low strain rate of 10^{-4} s^{-1}, the microstructure was characterized by dynamic recrystallization at the $\{10\bar{1}2\}$ extension, $\{10\bar{1}1\}$ contraction twins and grain boundaries. Twin dynamic recrystallization (TDRX), rotational dynamic recrystallization (RDRX) and discontinuous dynamic recrystallization (DDRX) were the main mechanisms responsible for the formation of recrystallized grains. The texture was characterized by the formation of three fibers: basal <0001>, $<10\bar{1}0>$// CD and $<11\bar{2}0>$ // CD where CD is the compression direction. Moreover, the texture was less sensitive to the deformation conditions since the recrystallized grains showed the same orientation than twins. The changes of the mechanical properties of the alloy were ascribed to the resulting microstructure due to the twinning and dynamic recrystallization.

Keywords: Dynamic recrystallization; PSC; Mg–Dy alloy; Texture; Twinning.

1. Introduction

Magnesium (Mg) based alloys are considered as the lightest structural materials (low density ∼ 1.74 g cm^{-3}) susceptible to be used in applications for the automotive and aerospace industries [1–3]. Unfortunately, Mg-based alloys suffer from poor formability at room temperature because of their hexagonal close-packed structure which limits the number of active deformation mechanisms [4]. In addition, the formation of a strong basal texture (i.e. {0002} basal planes are aligned parallel to the processing direction) during thermo-mechanical processing strongly affects their mechanical properties and limits their formability [5].

The plastic deformation of Mg-based alloys during deformation processing is limited to the two main mechanisms known as deformation by slip systems and mechanical twinning. The later one plays an important role in accommodating the deformation at low temperature since only basal slip occurs. Three common twin modes are often observed in deformed Mg-based alloys: $\{10\bar{1}2\}<10\bar{1}1>$ extension twin, $\{10\bar{1}1\}<10\bar{1}2>$ contraction twin and $\{10\bar{1}1\}$-$\{10\bar{1}2\}$ or $\{10\bar{1}3\}$-$\{10\bar{1}2\}$ double twins.

The extension and contraction twins can be activated for textured Mg-based alloys when the compression loading is applied perpendicular and along to the *c*-axis of the HCP unit

* Corresponding author.
E-mail address: hiba.azzeddine@univ-msila.dz (H. Azzeddine).

https://doi.org/10.1016/j.jma.2020.05.004

cell, respectively [6]. In contrast, the double twin is created by the formation of an extension twin inside a contraction one. The occurrence of extension twin is largely reported in Mg-based alloys than those of contraction and double twins due to their low critical resolved shear stress (CRSS) [7].

In fact, the presence of twins in the microstructure depends strongly on the alloying elements, initial texture, grain size and deformation conditions (temperature, strain rate and strain path) [8–13]. It is believed that the formation of twins during deformation strongly affects the flow stress and especially the texture by changing the orientation of the lattice structure [14,15]. Also, it is considered that extension and double twins are the principal twin type affecting the recrystallization behavior in Mg-based alloys [16,17]. For example, it was reported that the $\{10\bar{1}2\}$ extension twin represented a preferable site for the dynamic recrystallization (DRX) nucleation [18], while the $\{10\bar{1}1\}$-$\{10\bar{1}2\}$ double twin was found to be the preferred nucleation site for static recrystallization [19].

Mg-based alloys containing rare-earth elements (*RE*) showed excellent mechanical properties and good formability compared to conventional Mg-based alloys such as the AZ31 (Mg–3Al–1Zn, wt%) alloy [2,20]. The improvements were attributed to the effect of some *RE* elements on altering the basal texture development and changing the balance of activation of different slip systems and twinning [21,22].

Recent investigations have shown that the recrystallization behavior related to twinning was different from that of conventional Mg-based alloys [11,18,19]. However, the effects of *RE* elements on the dynamic recrystallization are more complicated than expected and much work is still needed in order to get a full understanding of recrystallization behavior and its relationship with deformation mechanisms.

Thus, the aim of the present study is to investigate the microstructural and textural evolution of the Mg–0.41Dy (wt%) alloy after plane strain compression (PSC) at 300 °C under a strain rate of 10^{-2} and 10^{-4} s^{-1} using electron backscatter diffraction (EBSD). The present results are discussed based on the effect of twinning and dynamic recrystallization mechanisms on the microstructure and texture development.

2. Experimental material and procedures

The as-cast Mg–0.41Dy alloy was kindly supplied by the Institute für Metallkunde und Metallphysik (IMM-RWTH) in Aachen, Germany. The alloy was produced by induction melting and casting under a protective gas atmosphere of Ar/CO_2 using preheated copper mold and followed by a partial solution annealing at 420 °C for 20 h.

Samples with dimensions of 14 mm (longitudinal direction, LD) × 10 mm (transverse direction, TD) × 6 mm (compression direction, CD) were machined from the as-cast bloc.

PSC tests were carried out at 300 °C under strain rates of 10^{-2} and 10^{-4} s^{-1} using a conventional screw-driven ZWICK testing machine as shown in Fig. 1. A final true strain of $\varepsilon = -1.2$ corresponding to 70% of thickness reduction was achieved for both samples.

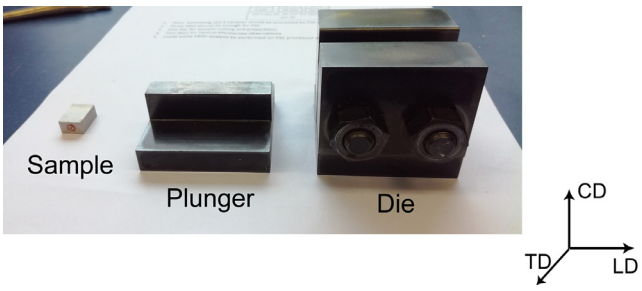

Fig. 1. Channel-die device used for PSC tests with the Mg–0.41Dy sample.

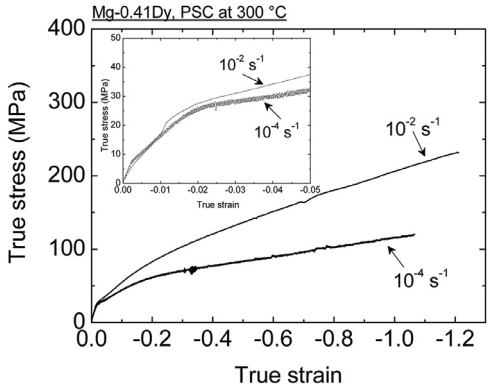

Fig. 2. True stress–strain curves of the Mg–0.41Dy deformed by PSC at 300 °C under a strain rate of 10^{-2} s^{-1} and 10^{-4} s^{-1}, respectively.

The microstructure of the samples was investigated in the LD-TD plane using EBSD after mechanical and ionic polishing using a Gatan PECS II system at a high voltage of 5 kV for 15 min. The EBSD data acquisition and analysis were undertaken using the TSL Orientation Imaging Microscopy, OIM™ software. The grain size data were obtained using a grain tolerance angle of 5° and the minimum grain size was chosen as 5 pixels.

Crystallographic texture was measured in the mid-thickness regions of the deformed samples (in the LD-TD plane) using a Phillips X-ray texture diffractometer. A set of six pole figures [$\{10\bar{1}0\}$, $\{0002\}$, $\{10\bar{1}1\}$, $\{10\bar{1}2\}$, $\{11\bar{2}0\}$, and $\{10\bar{1}3\}$] was measured to calculate the orientation distribution functions (ODF) using MTex software [23].

3. Results and discussions

3.1. PSC curves

Fig. 2 presents the true stress–strain curves of Mg–0.41Dy deformed by PSC at 300 °C under the strain rate of 10^{-2} s^{-1} and 10^{-4} s^{-1}. First, the stress increases rapidly in both samples mainly due to the work hardening resulting from the accumulation of dislocations. The magnified region of true strain in the range of 0–0.05 showed that both samples exhibit a sigmoidal hardening behavior typical for twin-assisted deformation [24]. It is evident that the sample deformed under high strain rate (10^{-2} s^{-1}) exhibited higher flow stress. This could be attributed to an enhanced activation of twin-

ning mode in the sample processed at high strain rate. It can be noticed that the true stress–strain curve of sample deformed under a strain rate of 10^{-4} s^{-1} shows massive serrations. It was demonstrated that the serration flow behavior was attributed to the DRX effects [25]. Moreover, the serration amplitude increases with decreasing strain rate [25]. The sample processed under high strain rate undergoes, in terms of 0.2% offset, higher yield strength (34 MPa) than the one at low strain (28 MPa). Then, the stress decreases slightly in the sample processed at low strain rate (10^{-4} s^{-1}) indicating a softening effect due to a DRX mechanism.

However, extensive secondary strain hardening can be noticed for strain up to −0.6 especially for sample processed at high strain rate. In fact, the secondary strain hardening is often reported in deformed Mg-based alloy by PSC such as WE54, AM50, AZ31 and ME20 alloys [5,26,27]. Consequently, it can conclude that the nature of alloying element could not be the reason for such behavior. Moreover, the development of twinning could not explain the second hardening since the twining occurrence in the earlier stage of the deformation [28]. The PSC deformation geometry (Fig. 1) is mostly the reason of this secondary hardening. First, the die prevents the sample broadening. Second, PSC test involved a significant amount of hydrostatic stress as a result of the friction between the sample and channel-die (as shown in Fig. 1). This friction effects would largely alter the hardening response and causes a false increase in work hardening [26].

The difference in the flow curves response of both samples is strongly related to the evolution of the deformation microstructure during the PSC test.

3.2. Microstructural evolution

Firstly, it should be mentioned that the microstructure of the as-cast alloy has been already reported and exhibits a random texture with very coarse grains (the average grain size is about 520 μm) [29]. Even if the solubility of Dy element in the Mg matrix is high (25.23%, wt%) [30], the as-cast microstructure showed the presence of $Mg_{24}Dy_5$ phase homogenously distributed in the microstructure [29]. Fig. 3(a) and (b) shows the microstructure as an orientation imaging micrography (OIM) in the inverse pole figure (IPF) map of the Mg–0.41Dy alloy after PSC at 300 °C under a stain rate of 10^{-2} and 10^{-4} s^{-1}, respectively. Both samples exhibit coarse elongated grains along LD and show the present of black zones resulting from the low degree of Kikuchi pattern quality due to the highly deformed areas in the samples. In addition, Fig. 3(c) and (d) presents the grains orientation spread (GOS) maps of the processed samples where GOS is defined as the mean standard deviation of all the orientations inside a grain [31]. The recrystallized grains (in blue) can be identified as grains having GOS values less than 2° [31]. As shown, both deformation microstructures exhibit dynamic recrystallized grains. A similar recrystallized fraction ∼ 20% was found for both processed samples. However, a net difference between the two samples concerning the presence of twins can be noticed. Indeed, they are manifestly more profuse in

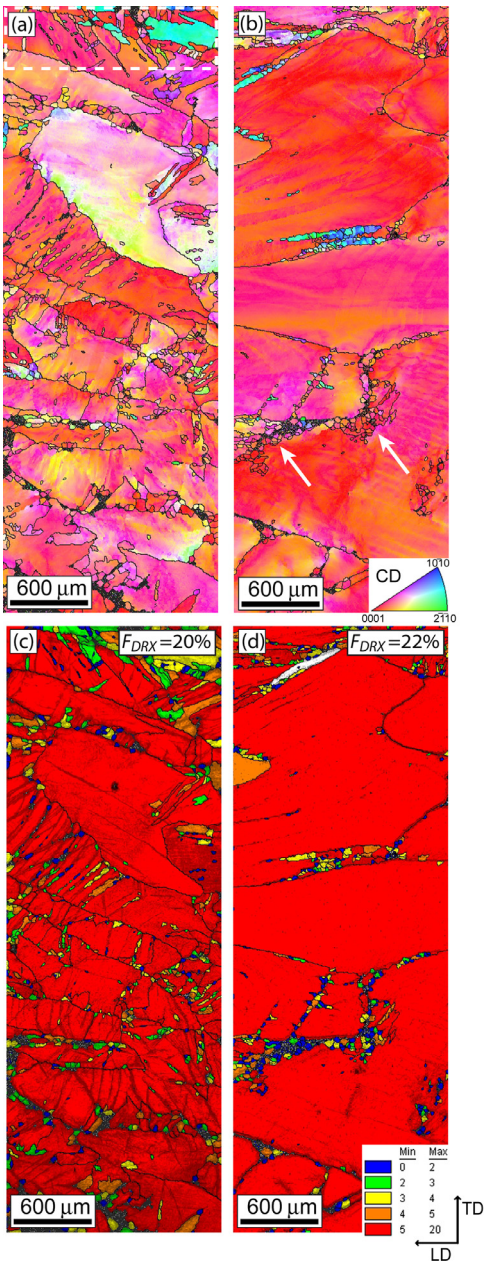

Fig. 3. CD-IPF and GOS maps of the Mg–0.41Dy alloy after PSC at 300 °C under a stain rate of: (a, c) 10^{-2} and (b, d) 10^{-4} s^{-1}.

the processed sample at stain rate of 10^{-2} s^{-1} (as indicated in the white box upper the Fig. 3(a)) than at 10^{-4} s^{-1}. This is in good agreement with the evolution of the flow stress curve shown in Fig. 2.

Table 1 shows the misorientation (angle/axis) between the identified twins and the parent grain and their fraction in both processed samples. Obviously, the three twinning mode are present in both deformed samples. The activation of the different twin modes in the same sample could be attributed to the random orientation of the grains in the as-cast alloy. The fraction of twins is higher in sample processed at high strain rate (10^{-2} s^{-1}). It is well known that twinning and basal slip are the predominated deformation mechanisms at the initial

Table 1
Fraction (F) of different twins identified in the deformed samples (from Fig. 3).

Twin mode	Misorientation (angle/axis)	F (%)	
		10^{-2} s^{-1}	10^{-4} s^{-1}
{10$\bar{1}$2} extension twin	86°<11$\bar{2}$0>	1.4	0.3
{10$\bar{1}$1}contraction twin	56°<11$\bar{2}$0>	1.0	0.3
{10$\bar{1}$1}{10$\bar{1}$2} double twin	38°<11$\bar{2}$0>	0.9	0.2
{10$\bar{1}$3}{10$\bar{1}$2} double twin	22°<11$\bar{2}$0>	2.2	1.5

stage of deformation. However, increasing temperature and decreasing strain rate renders twinning less important [32]. In this case, the dislocation density and their rearrangement may vary with strain rate and thence affect the twin nucleation and growth. In addition, for the low strain rate, it is assumed that twins can grow and eventually consume the entire parent grain, making them indistinguishable from the original matrix [24]. However, this statement may not be exact in the present study since as shown in Fig. 3(b) most grains are large and exhibit a basal texture (red color) indicating no changing in the orientation of grains caused by twinning. Hot deformation under low strain rate is more accommodated by dynamic recrystallization [33] as shown by the presence of small recrystallized grains along the grain boundaries as indicated by arrows in Fig. 3(b).

In order to visualize the different twin modes in sample processed under 10^{-2} s^{-1}, Fig. 4 has been drawn and shows the CD-IPF and the Image Quality (IQ) maps of selected regions from Fig. 3(a). Extension twin 86°<11$\bar{2}$0> (in green color), contraction twin 56°<11$\bar{2}$0> (red), double twin 38°<11$\bar{2}$0> (blue) and 22°<11$\bar{2}$0> (yellow) with an allowed angular spread of ± 8° are superposed in the IQ map. It is quite interesting to note that different twin modes can exist in the same grain. This is well expected since the nucleation of twin is strongly related to the grain boundary structure and the local stress state [34].

Table 1 and Fig. 4 show that double twin 22°<11$\bar{2}$0> and extension twin 86°<11$\bar{2}$0> dominate. The high fraction of double twin was attributed to the rapid transformation of contraction twin to double twin during deformation processing [35]. Nevertheless, the formation of double twins has been correlated with the local generation of voids and crack formation [36].

It is clear that the twins have different thicknesses and forms, especially for extension twin which have broader form than the others. The twin nucleation and growth rate depend strongly on several parameters such as the Schmid factor [37], the grain boundary misorientation distribution [37] and dislocations/twin boundary interactions [38]. Moreover, the corresponding {0002} pole figure shown in Fig. 4(c) demonstrated that the extension twin was able to change and/or create more different orientations than the contraction or double twin. Indeed, the c-axes of the extension twinned grains depicted a tilt angle of 86° from the basal plane of the parent grain which led to the development of {0002}//LD. Meanwhile, the contraction and double twin cause only the spread of basal plane toward TD.

Extension twin in the sample processed under low strain rate (10^{-4} s^{-1}) is presented in Fig. 5. The misorientation profile along the segment from A to B (Fig. 5(a)) shows that the misorientation angle between the parent grain and twin band is close to 86°. Moreover, the corresponding {0002} pole figure confirms the occurrence of extension twins, i.e. the {0002} basal planes of the twin band are oriented almost perpendicular to the CD. In contrast, the {0002} basal planes of the parent grain are parallel to the CD.

In fact, the twinned regions contain high stored energy and can act as favorable sites of dynamic recrystallization which known as twin-induced dynamic recrystallization (TDRX) mechanism [39]. Then, it appears that extension twin seems to act as a favorable site for the nucleation of dynamically recrystallized grains. The GOS map shown in Fig. 5(b) demonstrated actually the presence of recrystallized grains (in blue) inside the extension twin.

However, the interior of twin contains a high fraction of low grain boundaries, LAGBs (yellow and red lines) as presented in Fig. 5(c). These LAGBs will be progressively transformed to high grain boundaries (HAGBs) and therefore should form the new structure of fine recrystallized grains. This is in good agreement with the proposed mechanism of dynamic recrystallization nucleation in twin defined as a mutual intersection of the twins and the subdivision of the primary twin lamellae through LAGBs [39].

As evidenced from the {0002} pole figure, the orientations of dynamically recrystallized grains are the same than those of the host extension twin indicating a continuous dynamic recrystallization (CDRX) mechanism. Similar observations were reported on the recrystallized grains in contraction [40] and double twins [41]. However, recently, it has been reported that the recrystallized grains can develop different orientations from those of the host twins and parent grains [42,43]. Otherwise, the mechanism responsible for the nucleation and the orientation relationship between the recrystallized grains and the twins and parent grains is controversial and not fully understood yet.

Generally, the recrystallized grains inside contraction and double twins do not grow beyond twin boundaries due to their low mobilities which restricted the modification of the texture [19,42]. In contrast, it is expected that the recrystallized grains inside the extension twin will be able to grow since it is characterized by a high mobility [44].

Let us remark that no DRX was evidenced inside the twins formed in the sample processed under strain rate of 10^{-2} s^{-1} because of the short deformation duration (that is less than 10 min) since the recovery and the recrystallization are thermally activated processes. However, a TDRX mechanism was evidenced in AZ31 alloy processed by uniaxial compression at 200 °C and strain rate of 10^{-2} s^{-1} [33]. It was shown that

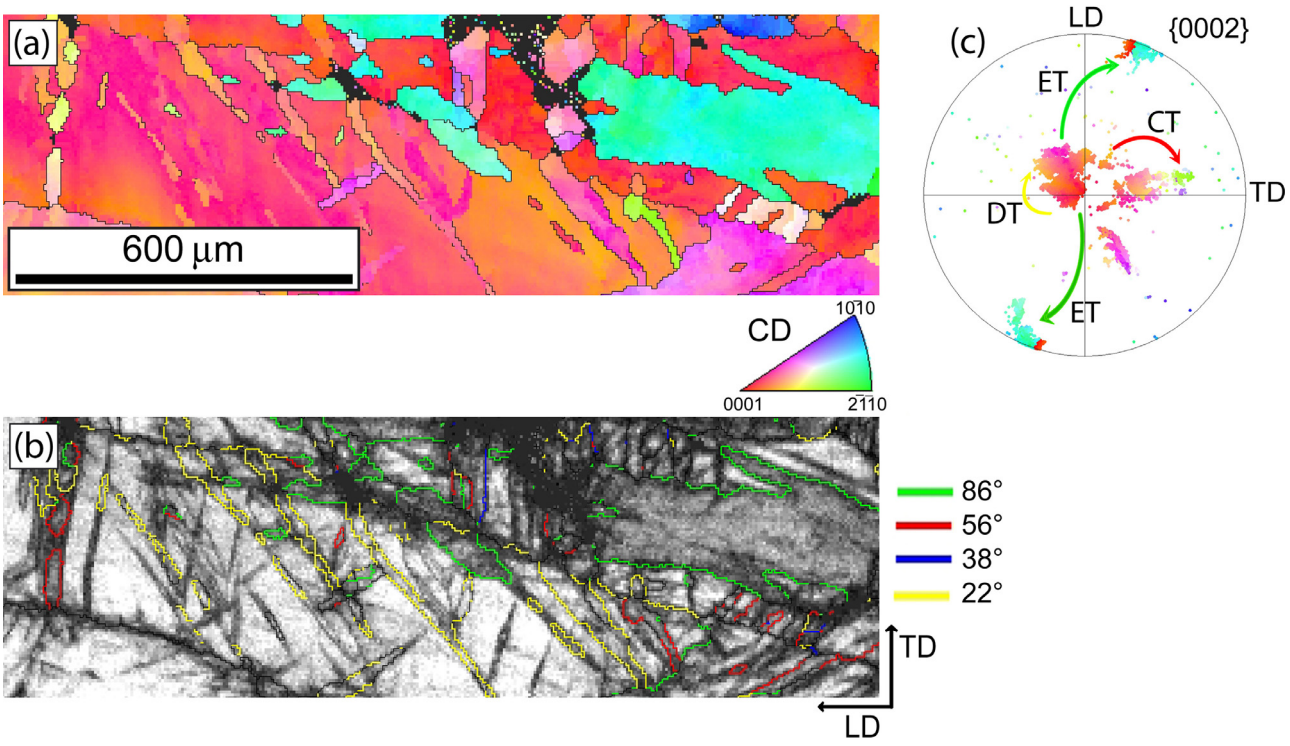

Fig. 4. (a) CD-IPF map of selected region of sample processed at 10^{-2} s^{-1} and (b) Image Quality (IQ) map showing the different twins. (c) The corresponding {0002} pole figure indicates the orientation between grains and twins. ET, CT and DT correspond to extension, contraction and double twins, respectively.

TDRX mechanism was induced due to the activation of non-basal slip system such as pyramidal $<c+a>$ slip [45].

Fig. 6 presents interesting microstructural features also observed in the sample processed at low strain rate (10^{-4} s^{-1}). It can be clearly seen that the large deformed grain (identified as number 1 in the figure) is surrounded by small grains ($\sim$ 35 μm) forming bands-like named as 'mantle' (shown by white lines). It was suggested that the formation of theses grains in bands resulted from the rotational dynamic recrystallization (RDRX) mechanism [46,47] rather than strain-induced boundary migration (SIBM) that is a conventional DRX mechanism. Accordingly, the new recrystallized grains started to form at the vicinity of grain boundaries ('mantle') due to the lack of deformation mode. With increasing strain, sub-grains formed in these mantle regions by dynamic recovery and HAGBs could ultimately be developed by the migration and coalescence of sub-boundaries, thereby forming new recrystallized grains [47].

It can be taken into consideration that the black zone in the Fig. 6(a) could be particles or second phases segregated at the grains boundaries. Obviously, this is not the case in the present alloy. First, the scanning electron microscopy (SEM) micrographs with different magnifications and the corresponding energy dispersive spectrometry (EDS) analysis of point 1 (Mg matrix) and 2 (particle) shown in Fig. 7 of the PSC processed sample at 10^{-4} s^{-1} indicate that the particles identified as $Mg_{24}Dy_5$ (point 2) are distributed into the whole microstructure and not at the grain boundaries. Second, the sizes of these particles were very small ($\sim$ 1.5 μm) compared to the black zone width in Fig. 6 ($\sim$ 40–60 μm). The SEM microstructures show also the presence of smaller particles (see arrows); however, their identification by EDS analysis was not possible. Finally, if the black zones were particles it is expected that the orientations of the recrystallized grains will be random as result of the simulated particle nucleation (PSN) mechanism [48]. As can be observed in Fig. 6(a) and (b) the orientations of the recrystallized grains in this region have exactly the same orientations of the deformed grains 1 and 3. However, further deeper investigations like using Transmission electron microscopy (TEM) measurements are needed to justify the occurrence of RDRX, SIBM or PSN mechanisms in the present Mg–0.41Dy alloy.

Fig. 6(c) shows the formation of new grains inside the contraction twin. However, the contraction twin was able to be identified only with angular spread of 30°. It was reported that the contraction twin lost its ideal 56° $<11\bar{2}0>$ misorientation relationship due to the occurrence of CDRX [40]. In the meantime, the recrystallized grains in this region exhibited wild orientations as shown in the {0002} pole figure (Fig. 6(b)).

Finally, the white arrows in Fig. 6(a) indicate that the grain boundaries were serrated and bulged which is indicative of a nucleation and formation of new DRX grains. The bulging at the grain boundaries is characteristic of the discontinuous dynamic recrystallization (DDRX) mode occurrence [49]. Usually, the DRX occurs during uniaxial compression (UC) and PSC starting from deformation temperature of 200 °C under high stain rate [24,33,50,51]. However, the microstructural evolution of the present alloy demonstrated clearly that DRX

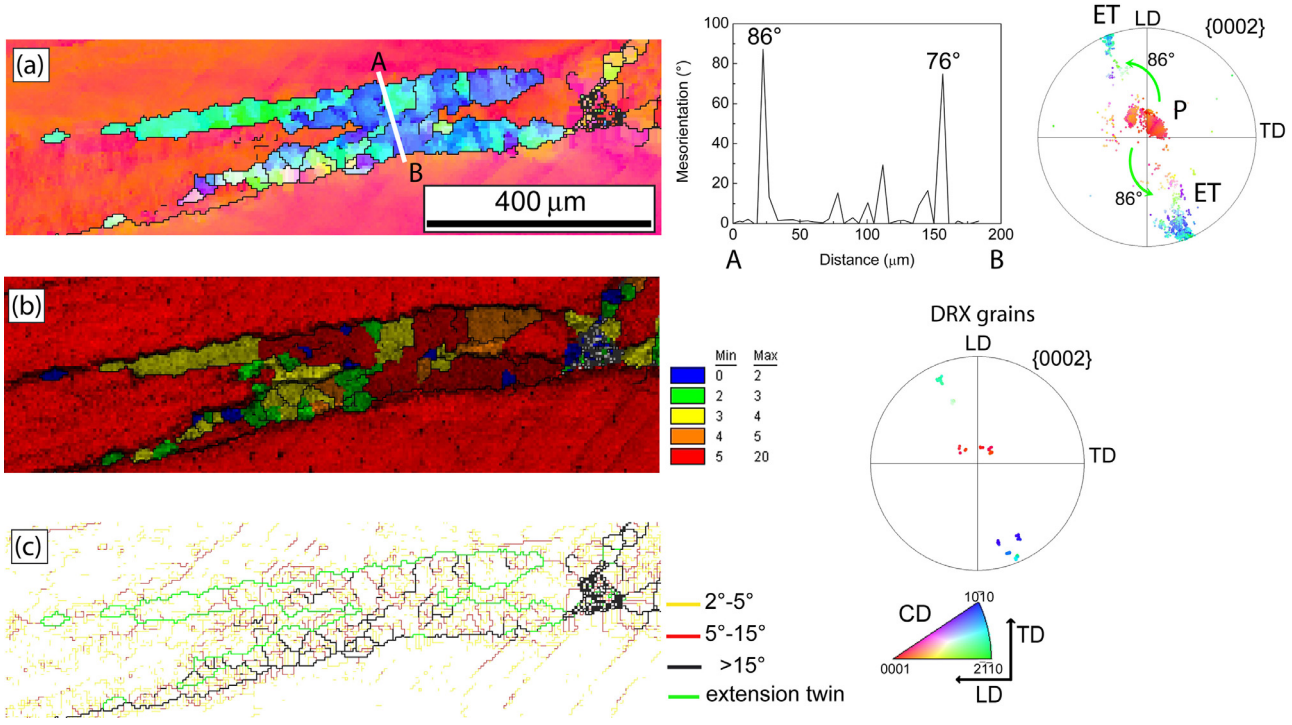

Fig. 5. (a) CD-IPF map and corresponding orientation marked in {0002} pole figure, (b) GOS map of selected region and {0002} pole figure of recrystallized grains and (c) Grain boundary map inside the extension twin observed in sample processed at 10^{-4} s^{-1}.

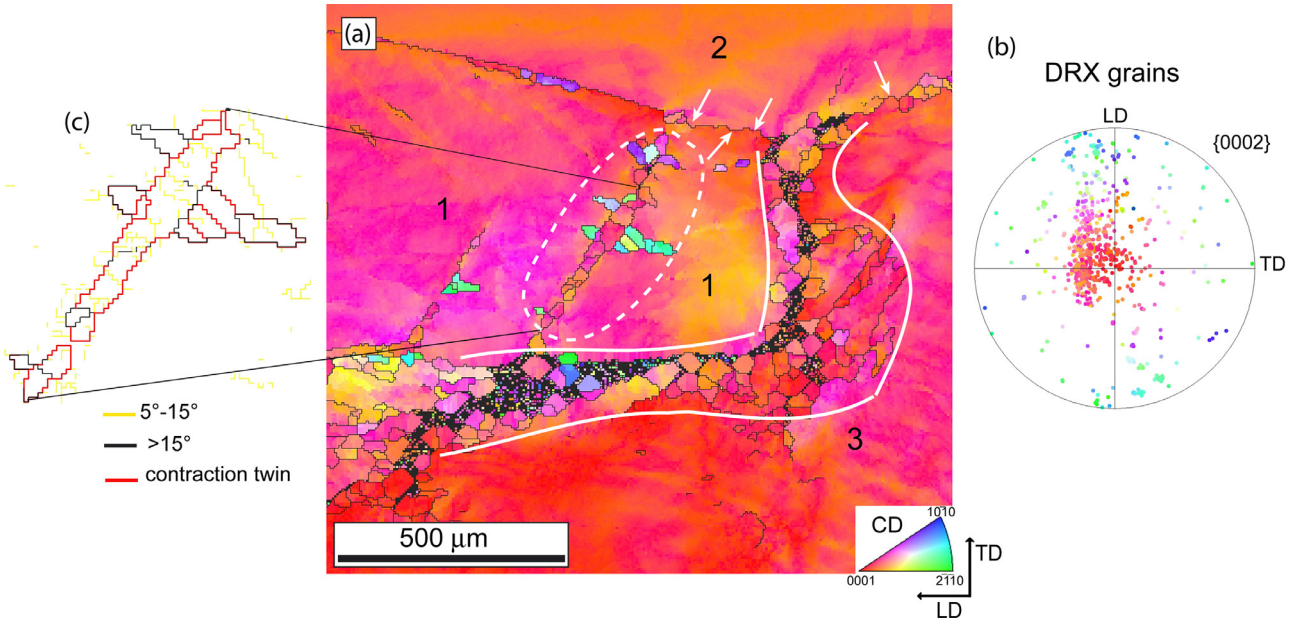

Fig. 6. (a) CD-IPF map of higher magnification region from Fig. 3(b) showing the recrystallized grains, (b) {0002} pole figure of the recrystallized grains and (c) Grain boundary map inside the small grains.

was very low at both processed samples. The occurrence of DRX at low temperature in conventional Mg-based alloy was attributed to the limitation of active slip system [24,33]. In case of Mg–RE alloy different slip system such as $<c+a>$ pyramidal slip can be easily activated due to the effect of RE elements and hence DRX is not anymore an important mechanism to accommodate the deformation. Moreover, the delay of DRX is also caused by RE solute drag at the grain boundaries (pinning effect) which result in reducing the grain boundary mobility [52].

3.3. Texture evolution

The macro-texture evolution obtained from XRD measurement of the Mg–0.41Dy alloy after PSC at 300 °C under a strain rate of 10^{-2} and 10^{-4} s^{-1} is shown in Fig. 8 via the

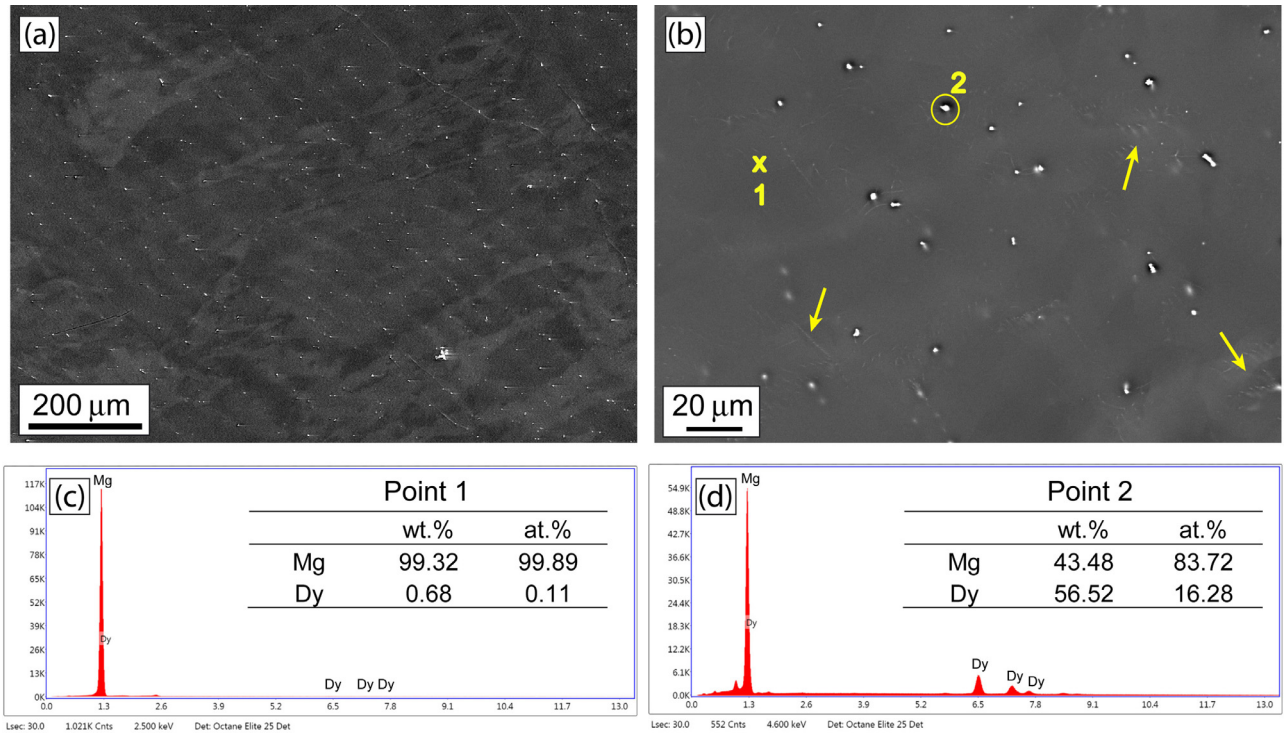

Fig. 7. (a, b) SEM micrographs with different magnifications and (c, d) the EDS results of point 1 and 2 of the PSC processed sample at strain rate of 10^{-4} s^{-1}.

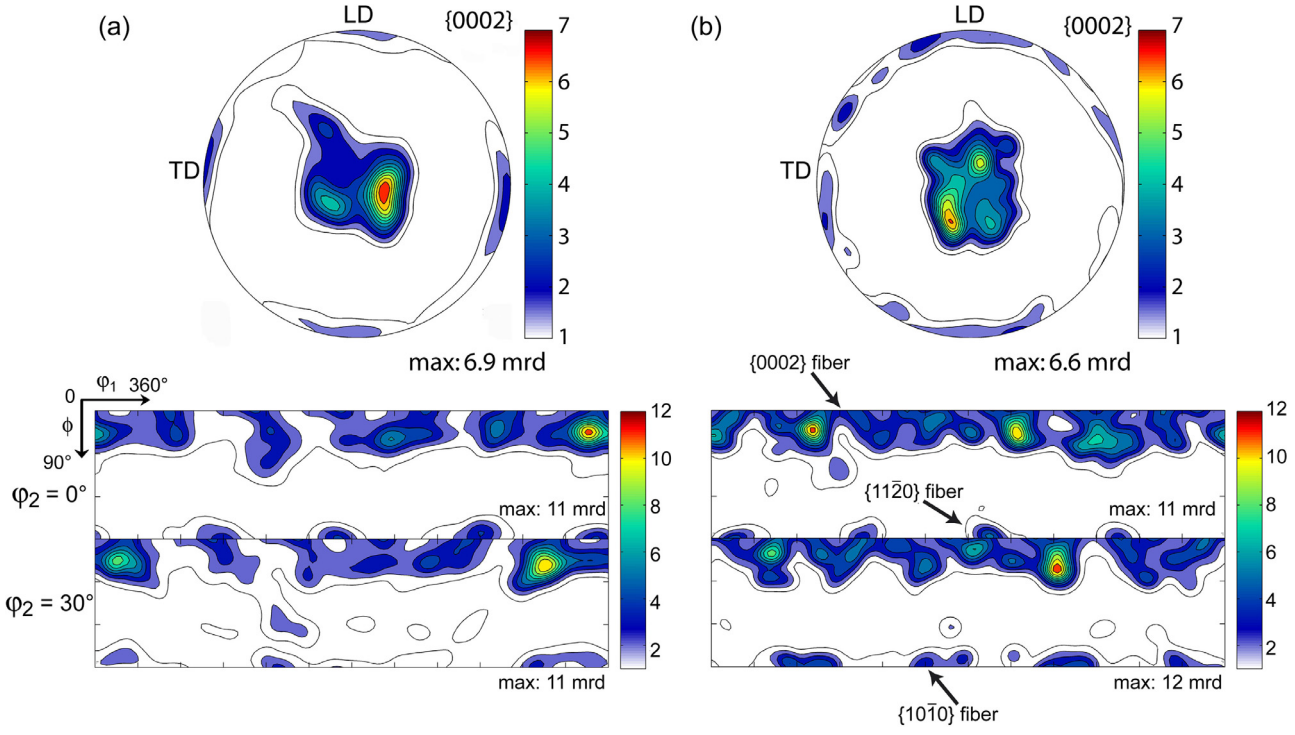

Fig. 8. Recalculated {0002} pole figure and ODF sections at $\varphi_2 = 0$ and 30° of the Mg–0.41Dy alloy after PSC at 300 °C and a strain rate of: (a) 10^{-2} and (b) 10^{-4} s^{-1}.

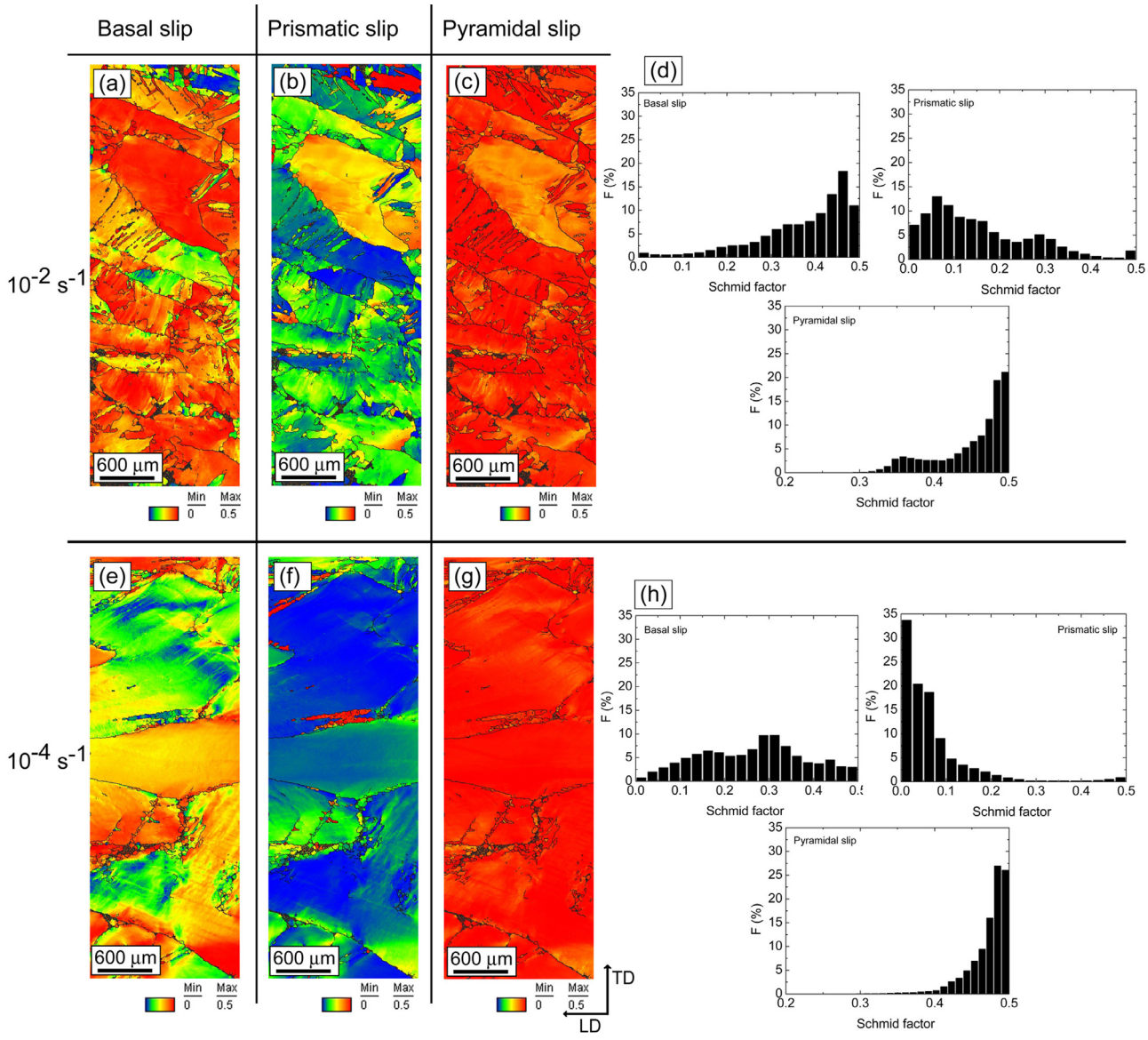

Fig. 9. SF distribution maps in tension along CD for the Mg–0.41Dy alloy after PSC at 300 °C under a stain rate of 10^{-2} s^{-1}: (a) basal, (b) prismatic, (c) pyramidal $<c+a>$ slip and under stain rate of 10^{-4} s^{-1}: (e) basal, (f) prismatic, (g) pyramidal $<c+a>$ slip and (d, h) the grain number fraction as a function of Schmid factor value for the different slip systems.

recalculated {0002} pole figure and ODF sections at $\varphi_2 = 0$ and 30°, respectively. As can be seen, PSC processing leads to the formation of three fibers: basal texture <0001> // CD ($\varphi_1 = 0$–360°, $\Phi = 0°$, $\varphi_2 = 0°$), $<10\bar{1}0>$ // CD ($\varphi_1 = 0$–360°, $\Phi = 90°$, $\varphi_2 = 30°$) and $<11\bar{2}0>$ // CD ($\varphi_1 = 0$–360°, $\Phi = 90°$, $\varphi_2 = 0°$). Similar texture evolution was reported in Mg–1.33La (wt%) alloy cold processed by PSC [53]. In contrast, hot PSC of the WE54 (Mg–4.9Y–4.2Nd–0.56Zr, wt%) alloy resulted in the formation only of *a* $<10\bar{1}0>$ // CD fiber [5]. Such a difference was attributed to the initial texture of the alloys. In the present studied alloy and the Mg–1.33La one from [53] both exhibited random textures prior to the deformation, while the WE54 alloy exhibited a basal texture [5]. The formation of $<10\bar{1}0>$ // CD fiber was caused by basal slip system since twinning may not be activated in alloys with initial basal texture (Schmid factor ~0) [5]. Thus, the formation of $<11\bar{2}0>$ // CD fiber is due to the activation of twinning as shown in the deformed microstructures.

Obviously, the strain rate has little effect on the texture formation and its intensity i.e. it is similar for both samples (~ 6–7 mrd, multiple of random distribution [54] for the {0002} pole figures and (~ 11–12 mrd for the ODF). However, the distribution of basal texture along LD and TD was different as function of strain rate. The split of basal poles is usually attributed to the activation of pyramidal $<c+a>$ slip system [55]. In addition, the $<10\bar{1}0>$ // CD and $<11\bar{2}0>$ // CD fibers seem to be more pronounced in the sample processed at low strain rate as indicated in the {0002} pole figures (Fig. 8). This could be attributed to occurrence of DRX with

different mechanisms and the formation of more off-basal texture.

It is interesting to elucidate the deformation behavior of the present deformed samples. The Schmid factor (SF) distribution obtained from the EBSD data measurement can be used to predict which slip modes can be favorably activated during deformation with specific loading direction [56]. Fig. 9 presents the SF distribution maps in tension along CD for Mg–0.41Dy alloy after PSC at 300 °C under stain rate of 10^{-2} s^{-1} and 10^{-4} s^{-1} for basal, prismatic, and pyramidal $<c+a>$ slip systems, respectively. The grain fraction as a function of SF value for different slip systems are also showed in the same figure. Usually, the SF values were classified into high (>0.3) and low (<0.3) values [57]. Accordingly, large amount of deformation can be accommodated by grains with high SF as compared to those with low SF values. It is obvious that the activation of basal and prismatic slip depends strongly on the imposed strain rate. The basal slip is more favored in sample processed at high strain rate (10^{-2} s^{-1}). In contrast, the prismatic slip has very SF low values in both samples, except for extension twin who exhibits high SF values as can be noticed (red color in Fig. 9(b) and (f)). In contrast, the pyramidal $<c+a>$ slip exhibits a high SF values for both samples.

The evolution of SF values confirms the statement that in Mg–RE alloys the pyramidal $<c+a>$ slip can be easily activated [21,22]. Although the deformation at elevated deformation temperatures allows the domination of the pyramidal $<c+a>$ slip as they can provide strain accommodation along the c-axis of grains [58].

4. Conclusion

- The microstructure and texture evolution of the as-cast Mg–0.41Dy alloy were investigated after PSC at 300 °C under different strain rates (10^{-2} and 10^{-4} s^{-1}) up to a final true strain of −1.2.
- The resulting microstructures due to twinning and dynamic recrystallization strongly influenced the flow behavior of the alloy.
- At high strain rate of 10^{-2} s^{-1}, the microstructure exhibited massive twins mainly extension, contraction and double twins due to the random orientations of the as-cast alloy.
- At low strain rate of 10^{-4} s^{-1}, the microstructure was characterized by dynamic recrystallization at the extension and contraction twins and at grain boundaries. TDRX, RDRX and DDRX were the main mechanisms responsible for the formation of recrystallized grains.
- The deformation texture was characterized by the formation of three fibers: <0001> // CD, $<10\bar{1}0>$ // CD and $<11\bar{2}0>$ // CD. Moreover, the texture was found to be not very sensitive to the deformation conditions.
- The evolutions of SF of basal, prismatic and pyramidal $<c+a>$ have similar trend for both processed samples.

Declaration of Interest

None.

Acknowledgments

Dr. Talal Al-Samman and his staff from the *Institut für Metallkunde und Metallphysik*, RWTH Aachen, are heartily acknowledged for providing the samples and their assistance. This work was supported by the PRFU national project under Grant Agreement No. B00L02UN280120180005.

References

[1] J. Hirsch, T. Al-Samman, Acta Mater. 61 (2013) 818–843, doi:10.1016/j.actamat.2012.10.044.
[2] A. Imandoust, C.D. Barrett, T. Al-Samman, K.A. Inal, H. El Kadiri, J. Mater. Sci. 52 (2017) 1–29, doi:10.1007/s10853-016-0371-0.
[3] S. You, Y. Huang, K.U. Kainer, N. Hort, J. Magnes. Alloys 5 (2017) 239–253, doi:10.1016/j.jma.2017.09.001.
[4] M.H. Yoo, Metall. Trans. A 12 (1981) 409–418, doi:10.1007/BF02648537.
[5] H. Azzeddine, D. Bradai, Int. J. Mater. Res. 11 (2012) 1351–1360, doi:10.3139/146.110768.
[6] S.H. Park, S.G. Hong, C.S. Lee, Scr. Mater. 62 (2010) 202–205, doi:10.1016/j.scriptamat.2009.10.027.
[7] M. Knezevic, A. Levinson, R. Harris, R.K. Mishra, R.D. Doherty, S.R. Kalidindi, Acta Mater. 58 (2010) 6230–6242, doi:10.1016/j.actamat.2010.07.041.
[8] M.R. Barnett, Woodhead Publishing Series in Metals and Surface Engineering, 2012, pp. 105–143.
[9] X. Liu, J.J. Jonas, L.X. Li, B.W. Zhu, Mater. Sci. Eng. A 583 (2013) 242–253, doi:10.1016/j.msea.2013.06.074.
[10] S.L. Shang, W.Y. Wang, B.C. Zhou, Y. Wang, K.A. Darling, L.J. Kecskes, S.N. Mathaudhu, Z.K. Liu, Acta Mater. 67 (2014) 168–180, doi:10.1016/j.actamat.2013.12.019.
[11] M. Arul Kumar, I.J. Beyerlein, R.A. Lebensohn, C.N. Tomé, Mater. Sci. Eng. A 706 (2017) 295–303, doi:10.1016/j.msea.2017.08.084.
[12] A. Chapuis, Q. Liu, Mater. Sci. Eng. A 725 (2018) 108–118, doi:10.1016/j.msea.2018.04.019.
[13] F. Abouhilou, A. Hanna, H. Azzeddine, D. Bradai, J. Magnes. Alloys 7 (2019) 124–133, doi:10.1016/j.jma.2018.11.003.
[14] X.Y. Yang, Z.S. Ji, H. Miura, T. Sakai, Trans. Nonferrous Metals Soc. China 19 (2009) 55–60, doi:10.1016/S1003-6326(08)60228-9.
[15] Y. Pei, A. Godfrey, J. Jiang, Y.B. Zhang, W. Liu, Q. Liu, Mater. Sci. Eng. A 550 (2012) 138–145, doi:10.1016/j.msea.2012.04.046.
[16] I. Basu, T. Al-samman, Acta Mater. 96 (2015) 111–132, doi:10.1016/j.actamat.2015.05.044.
[17] Z.-Z. Jin, X.-M. Cheng, M. Zha, J. Rong, H. Zhang, J.-G. Wang, C. Wang, Z.-G. Li, H.-Y. Wang, J. Mater. Sci. Technol. 35 (2019) 2017–2026, doi:10.1016/j.jmst.2019.05.017.
[18] S.H. Lu, D. Wu, R.S. Chen, E.-h. Han, J. Alloys Compd. 803 (2019) 277–290, doi:10.1016/j.jallcom.2019.06.279.
[19] D.K. Guan, W.M. Rainforth, L. Ma, B. Wynne, J.H. Gao, Acta Mater. 126 (2017) 132–144, doi:10.1016/j.actamat.2016.12.058.
[20] L.W.F. Mackenzie, F.J. Humphreys, G.W. Lorimer, K. Savage, T. Wilks, DGM, Germany, 2003, p. 158.
[21] K. Hantzsche, J. Bohlen, J. Wendt, K.U. Kainer, S.B. Yi, D. Letzig, Scr. Mater. 63 (2010) 725–730, doi:10.1016/j.scriptamat.2009.12.033.
[22] S. Sandlobes, S. Zaefferer, I. Schestakow, S. Yi, R. Gonzalez-Martinez, Acta Mater. 59 (2011) 429–439, doi:10.1016/j.actamat.2010.08.031.
[23] F. Bachmann, R. Hielscher, H. Schaeben, Solid. State Phenom. 160 (2010) 63–68, doi:10.4028/www.scientific.net/SSP.160.63.
[24] T. Al-Samman, X. Li, S.G. Chowdhury, Mater. Sci. Eng. A 527 (2010) 3450–3463, doi:10.1016/j.msea.2010.02.008.

[25] H. Azzeddine, D. Bradai, J. Rare Earths 31 (2013) 804–810, doi:10.1016/S1002-0721(12)60362-7.
[26] T. Al-Samman, Mater. Des. 65 (2015) 983–988, doi:10.1016/j.matdes.2014.10.025.
[27] X. Li, T. Al-Samman, S. Mu, G. Gottstein, Mater. Sci. Eng. A 528 (2011) 7915–7925, doi:10.1016/j.msea.2011.07.010.
[28] P. Chen, B. Li, D. Culbertson, Y. Jiang, Mater. Sci. Eng. A 709 (2018) 40–45.
[29] A. Hanna, H. Azzeddine, R. Lachhab, T. Baudin, A.L. Helbert, F. Brisset, Y. Huang, D. Bradai, T.G. Langdon, J. Alloys Compd. 778 (2019) 61–71, doi:10.1016/j.jallcom.2018.11.109.
[30] L. Rokhlin, Magnesium Alloys Containing Rare Earth Metals, Taylor and Francis, 2003.
[31] J.H. Cho, A. Rollett, K. Oh, Metall. Mater. Trans. A 36 (2005) 3427–3438, doi:10.1007/s11661-005-0016-4.
[32] C.N. Tomé, S.R. Agnew, W.R. Blumenthal, M.A.M. Bourke, D.W. Brown, G.C. Kaschner, P. Rangaswamy, Mater. Sci. Forum 408–412 (2002) 263–268, doi:10.4028/www.scientific.net/MSF.408-412.263.
[33] T. Al-Samman, G. Gottstein, Mater. Sci. Eng. A 490 (2008) 411–420, doi:10.1016/j.msea.2008.02.004.
[34] J. Wang, I.J. Beyerlein, C.N. Tomé, Scr. Mater. 63 (2010) 741–746, doi:10.1016/j.scriptamat.2010.01.047.
[35] S. Niknejad, S. Esmaeili, N.Y. Zhou, Acta Mater. 102 (2016) 1–16, doi:10.1016/j.actamat.2015.09.026.
[36] M.R. Barnett, Mater. Sci. Eng. A 464 (2007) 8–16, doi:10.1016/j.msea.2007.02.109.
[37] I.J. Beyerlein, L. Capolungo, P.E. Marshall, R.J. McCabe, C.N. Tomé, Philos. Mag. 90 (2010) 2161–2190, doi:10.1080/14786431003630835.
[38] F. Mokdad, D.L. Chen, D.Y. Li, J. Alloys Compd. 737 (2018) 549–560, doi:10.1016/j.jallcom.2017.12.043.
[39] O. Sitdikov, R. Kaibyshev, T. Sakai, Mater. Sci. Forum 419–422 (2003) 521–526, doi:10.4028/www.scientific.net/MSF.419-422.521.
[40] T. Al-Samman, K.D. Molodov, D.A. Molodov, G. Gottstein, S. Suwas, Acta Mater. 60 (2012) 537–545, doi:10.1016/j.actamat.2011.10.013.
[41] M. Wang, R. Xin, B. Wang, Q. Liu, Mater. Sci. Eng. A 528 (2011) 2941–2951, doi:10.1016/j.msea.2010.11.069.
[42] K.D. Molodov, T. Al-Samman, D.A. Molodov, G. Gottstein, Acta Mater. 76 (2014) 314–330, doi:10.1016/j.actamat.2014.04.066.
[43] J.H. Kim, B.-C. Suh, T.T.T. Trang, J.H. Hwang, N.J. Kim, Scr. Mater. 170 (2019) 11–15, doi:10.1016/j.scriptamat.2019.05.029.
[44] K.E. Prasad, K.T. Ramesh, Mater. Sci. Eng. A 617 (2014) 121–126, doi:10.1016/j.msea.2014.08.043.
[45] J.-X. Liu, K. Liu, W.-b. Du, S-b. Li, Z.-h. Wang, X. Du, C.-c. Sun, Trans. Nonferrous Met. Soc. China 28 (2018) 2214–2225, doi:10.1016/S1003-6326(18)64866-6.
[46] S.E. Ion, F.J. Humphreys, S.H. White, Acta Metall. 30 (1982) 1909–1919, doi:10.1016/0001-6160(82)90031-1.
[47] J.A. del Valle, M.T. Pérez-Prado, O.A. Ruano, Mater. Sci. Eng. A 355 (2003) 68–78, doi:10.1016/S0921-5093(03)00043-1.
[48] T. Al-Samman, Mater. Sci. Eng. A 560 (2013) 561–566, doi:10.1016/j.msea.2012.09.102.
[49] S.M. Fatemi-Varzaneh, A. Zarei-Hanzaki, H. Beladi, Mater. Sci. Eng. A 456 (2007) 52–57, doi:10.1016/j.msea.2006.11.095.
[50] G. Gottstein, T. Al Samman, Mater. Sci. Forum 495–497 (2005) 623–632, doi:10.4028/www.scientific.net/MSF.495-497.623.
[51] T. Al-Samman, Acta Mater. 57 (2009) 2229–2242, doi:10.1016/j.actamat.2009.01.031.
[52] I. Basu, K.G. Pradeep, C. Mießen, L.A. Barrales-Mora, T. Al-Samman, Acta Mater. 116 (2016) 77–94, doi:10.1016/j.actamat.2016.06.024.
[53] D. Elfiad, Y.I. Bourezg, H. Azzeddine, D. Bradai, Int. J. Mater. Res. 107 (2016) 315–323, doi:10.3139/146.111347.
[54] V. Randle, O. Engler, Introduction to Texture Analysis: Macrotexture, Microtexture and Orientation Mapping, CRC Press, 2000.
[55] M.T. Pérez-Prado, J.A. del Valle, J.M. Contreras, O.A. Ruano, Scr. Mater. 50 (2004) 661–665, doi:10.1016/j.scriptamat.2003.11.014.
[56] B.L. Wu, Y.H. Zhao, X.H. Du, Y.D. Zhang, F. Wagner, C. Esling, Mater. Sci. Eng. A 527 (2010) 4334–4340, doi:10.1016/j.msea.2010.03.054.
[57] J.J. Jonas, S. Mu, T. Al-Samman, G. Gottstein, L. Jiang, E. Martin, Acta Mater. 59 (2011) 2046–2056, doi:10.1016/j.actamat.2010.12.005.
[58] T. Al-Samman, B. Ahmad, G. Gottstein, Mater. Sci. Forum 550 (2007) 229–234, doi:10.4028/www.scientific.net/MSF.550.229.